Computations of Enhanced Soot Production in Time-Varying CH_4/Air Diffusion Flames

CAROLYN R. KAPLAN*
Laboratory for Computational Physics and Fluid Dynamics, Naval Research Laboratory, Washington, DC 20375

and

CHRISTOPHER R. SHADDIX† and KERMIT C. SMYTH
Building and Fire Research Laboratory, National Institute of Standards and Technology, Gaithersburg, MD 20899

Recent experimental measurements of soot volume fraction in a flickering CH_4/air diffusion flame show that for conditions in which the tip of the flame is clipped, soot production is ~5 times greater than that measured for a steady flame burning with the same mean fuel flow velocity (Shaddix et al., Ref. 9). This paper presents time-dependent numerical simulations of both steady and time-varying CH_4/air diffusion flames to examine the differences in combustion conditions which lead to the observed enhancement in soot production in the flickering flames. The numerical model solves the two-dimensional, time-dependent, reactive-flow Navier–Stokes equations coupled with submodels for soot formation and radiation transport. Qualitative comparisons between the experimental and computed steady flame show good agreement for the soot burnout height and overall flame shape except near the burner lip. Quantitative comparisons between experimental and computed radial profiles of temperature and soot volume fraction for the steady flame show good to excellent agreement at mid-flame heights, but some discrepancies near the burner lip and at high flame heights. For the time-varying CH_4/air flame, the simulations successfully predict that the maximum soot concentration increases by over four times compared to the steady flame with the same mean fuel and air velocities. By numerically tracking fluid parcels in the flowfield, the temperature and stoichiometry history were followed along their convective pathlines. Results for the pathline which passes through the maximum sooting region show that flickering flames exhibit much longer residence times during which the local temperatures and stoichiometries are favorable for soot production. The simulations also suggest that soot inception occurs later in flickering flames, and at slightly higher temperatures and under somewhat leaner conditions compared to the steady flame. The integrated soot model of Syed et al. (Ref. 12), which was developed from a steady CH_4/air flame, successfully predicts soot production in the time-varying CH_4/air flames.

NOMENCLATURE

a_{overall}	overall Planck mean absorption coefficient
C_v	heat capacity at constant volume
D	overall diffusion coefficient
$\overline{D}$	mean particle diameter
e	internal energy density
E	fluid energy density
f_v	soot volume fraction
G	gravitational acceleration
h_k	enthalpy of species k
ΔH_c	heat of combustion for CH_4
k	Boltzmann constant
k_A, k_B, k_T, k_Z	constants in Nagle and Strickland-Constable model
n	soot number density
n_k	species number density for species k
n_T	total number density
N_o	Avogadro's number
P_k	partial pressure of species k
P	pressure
Q	chemical heat release

* Corresponding author.
† National Research Council NIST Postdoctoral Research Associate, 1993–1995; present address: Combustion Research Facility, Sandia National Laboratories, Livermore, CA 94551.

0010-2180/96/$15.00
SSDI 0010-2180(95)00258-8

COMBUSTION AND FLAME 106: 392–405 (1996)

Published by Elsevier Science Inc.

q_c, q_r	thermal conductive and radiative heat flux
r	radial distance
R	universal gas constant
T	fluid temperature
T_∞	temperature of background gas
v_k	diffusion velocity of species k
v_t	thermophoretic velocity
t	time
V	fluid velocity
W_k	molecular weight of element k
W_{NSC}	oxidation rate, Nagle and Strickland-Constable model
X_k	mole faction of species k
Y_k	mass fraction of species k
z	axial distance
Z_k	mass fraction of element k

Greek Symbols

$C_\alpha, C_\beta, C_\gamma, C_\delta, T_\alpha, T_\gamma$	constants in Syed et al. soot formation model
β	weighted summation of atomic fractions
ξ	mixture fraction
ρ	fluid density
ρ_{soot}	density of a soot particle
σ	Stefan–Boltzmann constant
τ	viscous stress tensor
ν	kinematic viscosity
ω_k	source term for chemical reaction for species k
ω_n	source term for soot number density
ω_{f_v}	source term for soot volume fraction

INTRODUCTION

There have been numerous studies over the past two decades on the use of numerical models to simulate steady laminar diffusion flames. However, many practical flames are unsteady, and increased attention has focused on the development of time-dependent models to adequately characterize the fluctuating behavior of these flames. Time-dependent numerical simulations of unsteady hydrogen-air jet diffusion flames have investigated the effects of heat release, viscosity, and gravity on the development and dynamics of the high-frequency Kelvin–Helmholtz instabilities in the inner shear layer of the jet and on the low-frequency, buoyancy-driven outer structures [1, 2]. The role of buoyancy in the formation of the low-frequency outer structures was also investigated for propane/air jet diffusion flames [3, 4]. Other time-dependent simulations have examined the effects of nonunity Lewis number and finite-rate chemistry on the dynamics of hydrogen/air flames [5] and studied the vortex–flame interactions in CH_4/air jet diffusion flames [6].

Since many practical combustion conditions involve sooting hydrocarbon diffusion flames, recent efforts have focused on the development of a time-dependent numerical model which includes the processes of soot formation and radiation transport. An investigation of the effects of multidimensional radiation transport in a heavily sooting ethylene jet diffusion flame demonstrated how radiative losses change the overall temperature, species concentration, and soot volume fraction distributions [7]. This numerical model has also been used to investigate the fluid-chemical interactions and the role of the inner shear-layer instabilities in lifted methane/air jet diffusion flames [8].

The purpose of the present paper is to apply these newly developed modeling capabilities to study soot production in time-varying methane/air diffusion flames. Recent experimental measurements in a flickering CH_4/air flame show that for conditions in which the tip of the flame is clipped, the peak local soot volume fraction is 5–6 times greater than that measured for a steady flame burning with the same mean fuel flow velocity [9, 10]. Time-varying diffusion flames exhibit different combinations of residence time, temperature history, strain rate, and local stoichiometry than those

observed in steady flames. A computational investigation of how these key parameters affect soot production and destruction can provide new insight into the fluid–chemical interactions which result in the dramatically enhanced soot production experimentally observed in time-varying flames.

Formulations of integrated soot models (wherein soot inception, growth, agglomeration, and oxidation processes are included) is an active area of combustion research [11–21]. These descriptions have been perforce developed using experimental data from steady diffusion flames, but the goal is their application to turbulent combustion conditions. The flickering flame measurements offer demanding tests of such integrated soot models for a reproducible, yet complex combusting flowfield. For methane combustion the soot model of Syed et al. [12] is of particular interest, since soot production and destruction are described simply in terms of the local temperature and methane mole fraction. As such, this model can be easily incorporated into a time-dependent simulation.

Here direct numerical simulations are presented in order to (a) quantitatively compare experimental soot volume fraction and temperature results for a steady CH_4/air flame with predictions, (b) compare experimental measurements and computations of the soot volume fraction in the flickering flames, and (c) elucidate the changes in residence time, temperature, and mixture fraction which lead to the enhanced soot production observed in the flickering flames.

NUMERICAL METHOD

The numerical model solves the two-dimensional, axisymmetric, time-dependent, reactive-flow Navier–Stokes equations coupled with submodels for soot formation and radiation transport:

$$\frac{\partial \rho}{\partial t} + \nabla \cdot (\rho V) = 0, \tag{1}$$

$$\frac{\partial \rho V}{\partial t} + \nabla \cdot (\rho VV) = -\nabla P + \rho G - \nabla \cdot \tau, \tag{2}$$

$$\frac{\partial E}{\partial t} + \nabla \cdot (EV) = -\nabla \cdot PV - \nabla \cdot (q_c + q_r) - \nabla \cdot \sum n_k v_k h_k + Q, \tag{3}$$

$$\frac{\partial n_k}{\partial t} + \nabla \cdot (n_k V) = -\nabla \cdot (n_k v_k) + \omega_k, \tag{4}$$

$$\frac{\partial n}{\partial t} + \nabla \cdot (nV) = -\nabla \cdot (v_t n) + \omega_n, \tag{5}$$

$$\frac{\partial f_v}{\partial t} + \nabla \cdot (f_v V) = -\nabla \cdot (v_t f_v) + \omega_{f_v}. \tag{6}$$

Equations 1–6 are closed by the ideal gas relations:

$$P = n_T kT \tag{7}$$

$$de = \rho C_v \, dT. \tag{8}$$

Equations 1–4 include terms for convection, thermal conduction, molecular diffusion, viscosity, chemical reaction and energy release, gravity, and radiation transport. The soot conservation equations, Eqs. 5 and 6, include terms for convection and thermophoresis, where the thermophoretic velocity is defined by

$$v_t = -0.54\nu \frac{\nu \ln T}{\partial r}. \tag{9}$$

Our solution to Eqs. 1–6 includes both the radial and axial components of the convective and diffusive transport terms (thermal conduction, molecular diffusion, and viscosity). However, only the radial component of the thermophoretic term is considered in Eqs. 5 and 6, and only the axial component of the gravitational acceleration term is included in Eq. 2. These equations are then rewritten in terms of finite-difference approximations on an Eulerian mesh and solved numerically for specified boundary and initial conditions. The model consists of separate algorithms for each of the individual processes, which are then coupled together by the method of timestep splitting [22].

The present model uses the same algorithms for the convective and diffusive transport processes as previously published [1, 2, 7, 8] and therefore will only be briefly described here. The algorithms for chemical reaction/energy release, soot formation and oxidation, as well as radiation transport, are different than those

published previously and are discussed in more detail below.

Convective and Diffusive Transport

Fluid convection is solved with a high-order implicit algorithm, Barely Implicit Correction to Flux-Corrected Transport (BIC-FCT), that was developed by Patnaik et al. [23] to solve the convection equations for low-velocity flows. The Flux-Corrected Transport (FCT) algorithm [22] itself involves an explicit, finite-difference method that is constructed to have fourth-order phase accuracy. However, because FCT is an explicit algorithm, the numerical timestep required for accuracy and stability is limited by the velocity of sound. The basic approach used in BIC-FCT is to treat only those terms whose accuracy and stability are limited by the sound speed (such as the pressure terms in the momentum and energy equations) implicitly.

Thermal conduction, molecular diffusion, and viscosity are evaluated using explicit two-dimensional finite differencing [1, 2, 7, 8]. The algorithm for molecular diffusion includes multicomponent diffusion among all species tracked (CH_4, O_2, H_2O, CO_2, and N_2), where the binary diffusion coefficients are calculated as a function of temperature for each species-pair from kinetic theory using Lennard–Jones parameters from the Sandia Transport Data Base [24]. Similarly, the thermal conduction and viscosity coefficients are also calculated from kinetic theory for each individual species as a function of temperature. Using mixture rules [1, 2, 7, 8], an overall mixture thermal conductivity, mixture viscosity coefficient, and mixture diffusion coefficient are then calculated from the species coefficients in each computational cell. The viscosity sub-model includes all of the viscous terms in the compressible Navier-Stokes equations. Subcycling is used in the molecular diffusion and thermal conduction modules to ensure numerical stability.

Chemical Reaction and Energy Release

Due to the large amount of computational time required to solve the conservation equations over a highly-resolved computational grid (up to 40 h on a Cray YMP for the flickering flame calculations, which required 60,000 to 80,000 timesteps to reach convergence), a simplified chemical reaction/energy release model was used. In contrast to previous calculations which incorporated global chemical rates derived from premixed reaction data [1, 2, 7], the present computation utilized a fuel consumption rate based on Bilger's [25] formulation for chemical reaction in diffusion flames:

$$\omega_{CH_4} = -\rho D(\nabla\xi)^2 \frac{d^2 Y_{CH_4}}{d\xi^2}, \tag{10}$$

where D is an overall diffusion coefficient [26], (cm^2/s),

$$D = 1.786 \times 10^{-5} T^{1.662}. \tag{11}$$

Mixture fraction is expressed in the form

$$\xi = \frac{\beta - \beta_2}{\beta_1 - \beta_2}, \tag{12}$$

where β is a weighted summation of atomic fractions [27] and the subscripts 1 and 2 refer to the fuel and oxidizer streams, respectively:

$$\beta = 2\frac{Z_C}{W_C} + 0.5\frac{Z_H}{W_H} - \frac{Z_O}{W_O}. \tag{13}$$

Equation 10 is derived from the chemical species conservation equation by making a number of assumptions which could seemingly lead to pitfalls in practice, including (a) equal binary diffusion coefficients, $D_{i,j} = D$, (b) D = constant, and (c) species mass fractions described as unique functions of the mixture fraction, $Y_i = Y_i(\xi)$. In spite of these potential problems recent comparisons of reaction rates derived from Eq. 10 and those calculated from direct numerical simulation (with a detailed chemical mechanism) of a methane/air diffusion flame show good agreement for the major species [28]. Although this chemical reaction sub-model is based on the assumption of equal and constant binary diffusion coefficients, our molecular diffusion sub-model does include multi-component species diffusion (as discussed in the preceeding section).

The species tracked include O_2, CO_2, H_2O, and N_2 (assumed to be chemically inert). After the CH_4 consumption rate is calculated from

Eq. 10, the consumption rate of O_2 and the production rates of CO_2 and H_2O are then evaluated from their respective stoichiometric coefficients. The amount of heat released is then calculated from

$$Q = -\Delta H_c \frac{d[CH_4]}{dt}. \tag{14}$$

Soot Formation and Radiation Transport

The thermophoretic term which appears in the conservation equations (Eqs. 5 and 6) is solved with explicit finite differencing. The source terms in Eqs. 5 and 6 are represented by a set of two coupled ordinary differential equations in terms of the soot number density and the soot volume fraction. These quantities are computed as a function of the local gas properties based upon the simplified rate expressions of Syed et al. [12], which were developed from measurements in a steady CH_4/air flame:

$$\omega_n = \frac{dn}{dt} = C_\alpha N_o \rho^2 T^{1/2} X_{\text{fuel}} e^{-T_\alpha/T} - \frac{C_\beta}{N_o} T^{1/2} n^2 - \frac{(36\pi)^{1/3} W_{\text{NSC}} n^{4/3}}{\rho_{\text{soot}} f_v^{1/3}} \tag{15}$$

$$\omega_{f_v} = \frac{df_v}{dt} = \frac{C_\delta}{\rho_{\text{soot}}} C_\alpha \rho^2 T^{1/2} X_{\text{fuel}} e^{-T_\alpha/T} + \frac{C_\gamma}{\rho_{\text{soot}}^{1/3}} \rho T^{1/2} X_{\text{fuel}} e^{-T_\gamma/T} n^{1/3} f_v^{2/3} - \frac{(36\pi)^{1/3} W_{\text{NSC}} n^{1/3} f_v^{2/3}}{\rho_{\text{soot}}}, \tag{16}$$

where the soot particle density, ρ_{soot}, is assumed to be 1.8 g/cm^3, and the coefficients and activation temperatures are

$C_\alpha = 6.54 \times 10^4$ cm^3/g$^2 \cdot$ K$^{1/2} \cdot$ s,

$C_\beta = 1.3 \times 10^{13}$ cm^3/K$^{1/2} \cdot$ s,

$C_\gamma = 1.0 \times 10^3$ cm^3/g$^{2/3} \cdot$ K$^{1/2} \cdot$ s,

$C_\delta = 1.44 \times 10^5$ g,

$T_\alpha = 4.61 \times 10^4$ K,

$T_\gamma = 1.26 \times 10^4$ K.

The first and second terms on the right-hand side of Eq. 15 correspond to inception and coagulation, while the first and second terms in Eq. 16 represent inception and surface growth. The third term on the right hand side of Eqs. 15 and 16 represents soot oxidation, and has been added here to the original expression of Syed et al. [12]. This term includes only the Nagle and Strickland-Constable (NSC) [29] rate for oxidation by O_2 (g/cm$^2 \cdot$ s),

$$W_{\text{NSC}} = 12\left\{\frac{k_A P_{O_2}}{1 + k_z P_{O_2}} \chi + k_B P_{O_2}(1 - \chi)\right\}, \tag{17}$$

where

$$\chi = \frac{1}{1 + \dfrac{k_T}{k_B P_{O_2}}} \tag{18}$$

and

$k_A = 20 \exp(-30000/RT)$ g/cm$^2 \cdot$ s $\cdot$ atm,

$k_B = 4.46 \times 10^{-3} \exp(-15200/RT)$ g/cm$^2 \cdot$ s $\cdot$ atm,

$k_T = 1.51 \times 10^5 \exp(-97000/RT)$ g/cm$^2 \cdot$ s,

$k_Z = 21.3 \exp(4100/RT)$ 1/atm.

The other variables and factors in the oxidation terms in Eqs. 15 and 16 are used to convert the NSC oxidation rate into appropriate units for the set of ordinary differential equations. In these computations both the soot volume fraction, f_v, and the number density, n, are tracked, and therefore a mean surface area per unit volume, $n\pi\bar{D}^2 = (36\pi)^{1/3} n^{1/3} f_v^{2/3}$, can be determined. The oxidation rate in units of mass loss rate per unit volume (g/cm$^3 \cdot$ s) is given by $W_{\text{NSC}} \cdot (36\pi)^{1/3} n^{1/3} f_v^{2/3}$. The oxidation rate in terms of the soot volume fraction (third term in Eq. 16) is obtained by dividing this last expression by ρ_{soot}. To find the oxidation rate in terms of number density, this expression is divided by ρ_{soot} and by the mean particle volume, f_v/n.

A recent review [30] of soot oxidation measurements analyzed in terms of the Nagle and

Strickland-Constable expression concluded that the NSC rate is likely to overestimate soot oxidation due to O_2 at temperatures below 1800 K and possibly underpredicts the O_2 contribution at higher temperatures. In addition, Puri et al. [30] found that the OH · radical is as important for soot oxidation as O_2 in steady, axisymmetric hydrocarbon diffusion flames. These effects are offsetting for $T < 1800$ K, but on balance one expects that the NSC expression for soot oxidation will underpredict actual soot oxidation rates for the CH_4/air flames under investigation here.

Because methane is a relatively weakly sooting fuel, the radiation transport sub-model uses an optically-thin assumption,

$$-\nabla \cdot q_r = 4a_{\text{overall}}\sigma(T^4 - T_\infty^4), \tag{19}$$

where σ is the Stefan–Boltzmann constant. The absorption coefficient for soot (cm^{-1}) is based on an expression from Kent and Honnery [31], while that for CO_2 and H_2O is taken from Magnussen and Hjertager [32]. These are then combined to form an overall Planck mean absorption coefficient:

$$a_{\text{overall}} = 2.66 \cdot \text{const} \cdot f_v \cdot T + 0.001(X_{CO_2} + X_{H_2O}). \tag{20}$$

RESULTS

Computational Domain and Boundary Conditions

Figure 1 shows the computational grid and a schematic of the initial flow and boundary conditions for the computations. The full computational domain consists of 128 × 152 cells and covers an area of 10 cm (radially) by 20 cm (axially). Cells of 0.02 cm × 0.02 cm are concentrated around the lower and left-hand boundaries (where the flame is located), and the grid is then stretched both radially and axially. To match the experimental conditions

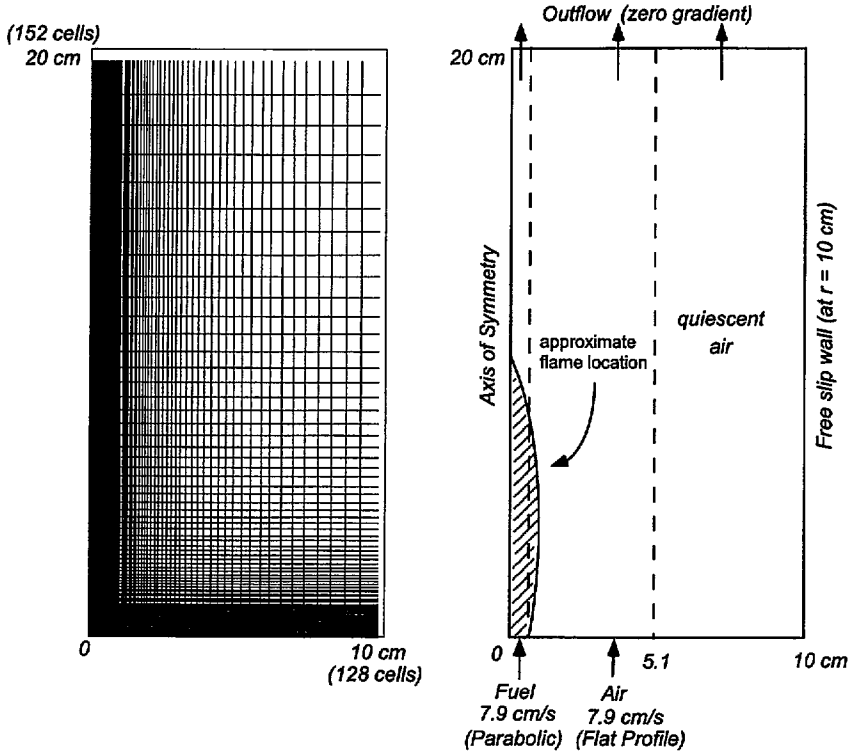

Fig. 1. Grid and schematic of the computational domain and boundary conditions; every other line in the computational grid is shown. The fuel velocity of 7.9 cm/s is the area-averaged velocity.

of Refs. 9 and 10, the fuel and air cold flow velocities are both 7.9 cm/s for the steady flame calculation, with the fuel tube radius 0.55 cm and the air annulus radius 5.1 cm. The full computational domain is extended out to 10 cm radially and contains quiescent air from 5.1 to 10 cm radially. Extending the radial computational domain minimizes the effects of the right-hand boundary condition on the computed flame. The fuel and air are preheated to 550 K and 330 K, respectively, based upon experimental thermocouple measurements for a series of heights just above the burner [33]. These data were extrapolated to estimate the temperature at the burner exit. The conditions modeled include parabolic pipe flow for the fuel and a flat velocity profile for the coflowing air stream at the inflow boundary, flat thermal profiles for the fuel and air streams, symmetry at the left-hand boundary, free-slip wall at the right-hand boundary, and zero-gradient (simple continuative) outflow condition at the top of the computational domain.

Steady Methane / Air Flame

Although a time-dependent simulation was conducted, the results from the computations successfully matched experimental steady-state conditions after 16000 timesteps (0.16 s). Local soot volume fractions have been measured using tomographic reconstruction of extinction data obtained at 632.8 nm as well as laser-induced incandescence (LII) line images, with the LII method providing superior signal-to-noise [9]. Temperatures have been obtained from radiation-corrected thermocouple data [33]. Figure 2 shows both the measured OH · fluorescence and soot scattering signals along with the computed temperature and soot volume fraction. These *qualitative* comparisons exhibit similar wishbone flame shapes and overall flame heights.

Quantitative comparisons between the experimental and computed profiles of temperature, presented in Fig. 3a, reveal good agreement at mid-flame heights: 30 and 50 mm above the fuel tube exit. However, the computations underpredict the flame diameter at very low (7 mm) and high (70 mm) axial locations. Comparisons between the experimental and computed soot volume fraction, Fig. 3b, exhibit good agreement for the radial location of the peak soot volume fraction at all heights, and excellent quantitative agreement for the maximum soot concentrations in the flame (within 15%) at heights of 50–70 mm. Discrepancies between the predicted and measured conditions at low heights can be partially attributed to the inflow boundary, which does not include the actual burner lip and hence neglects any interactions occurring between the flame and the metal fuel tube. Experimentally, the fuel tube extends 4 mm above the ceramic honeycomb used to straighten the air flow [34], and the OH · region is observed to attach to the outer edge of this tube (Fig. 2). The current state of the implicit flow solver does not allow such a type of boundary; however, efforts are underway to modify this condition.

In the upper flame region where soot is oxidized, the Nagle and Strickland-Constable rate expression for O_2 performs surprisingly well, considering that the oxidation of soot by OH · is also important [30]. At a height of 80 mm (not shown in Fig. 3b) the computed peak soot volume fraction is 4.0×10^{-8}, while the experimental measurements (sensitive to $f_v = 5 \times 10^{-9}$) do not detect any soot; the observed visible flame height is 79 mm. This indicates that the NSC expression predicts a somewhat slower rate of soot burnout than is observed at the very top of the flame. However, Fig. 4 shows good agreement between the experimental and computed flame height in terms of the area-integrated soot volume fraction. The computed soot volume fraction over the entire flame is slightly larger than the experimental measurement, due to a wider computed soot layer thickness (Fig. 3b). The overall agreement between the experimental and computed soot volume fraction profiles compares favorably to prior studies, even where the computed results have been plotted against the experimental steady flame data used to develop an integrated soot model [11–18, 20, 21].

Experimental measurements and computations of the soot volume fraction have also been made for a taller, steady CH_4/air diffusion flame for which the fuel and air cold flow velocities are 10.1 and 13.0 cm/s, respectively. Puri et al. [30] investigated soot oxidation rates

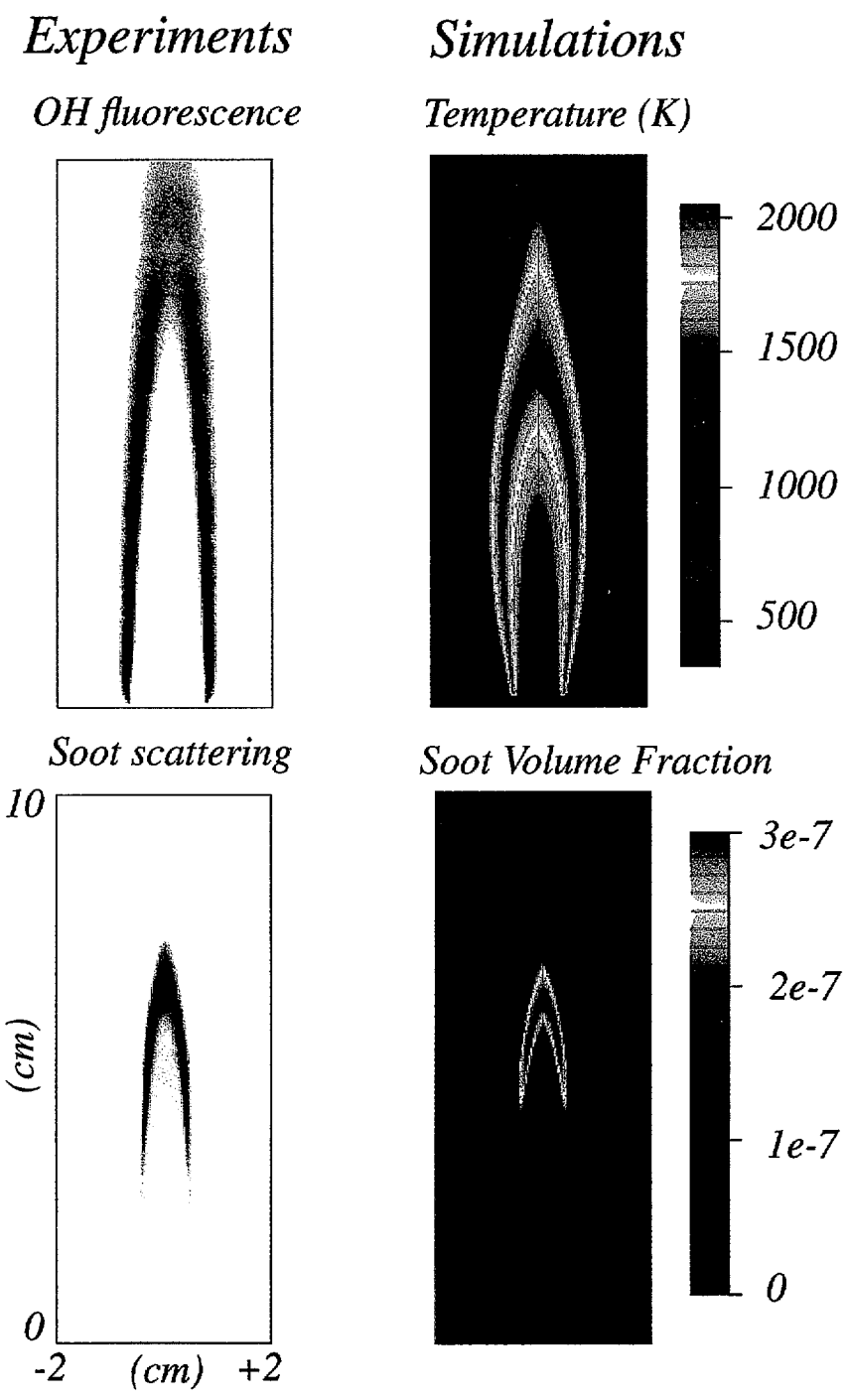

Fig. 2. Qualitative comparisons between the experimental and computed steady CH_4/air diffusion flame (7.9 cm/s fuel flow velocity): experimentally measured OH• fluorescence versus computed temperature, and experimentally measured soot scattering versus computed soot volume fraction.

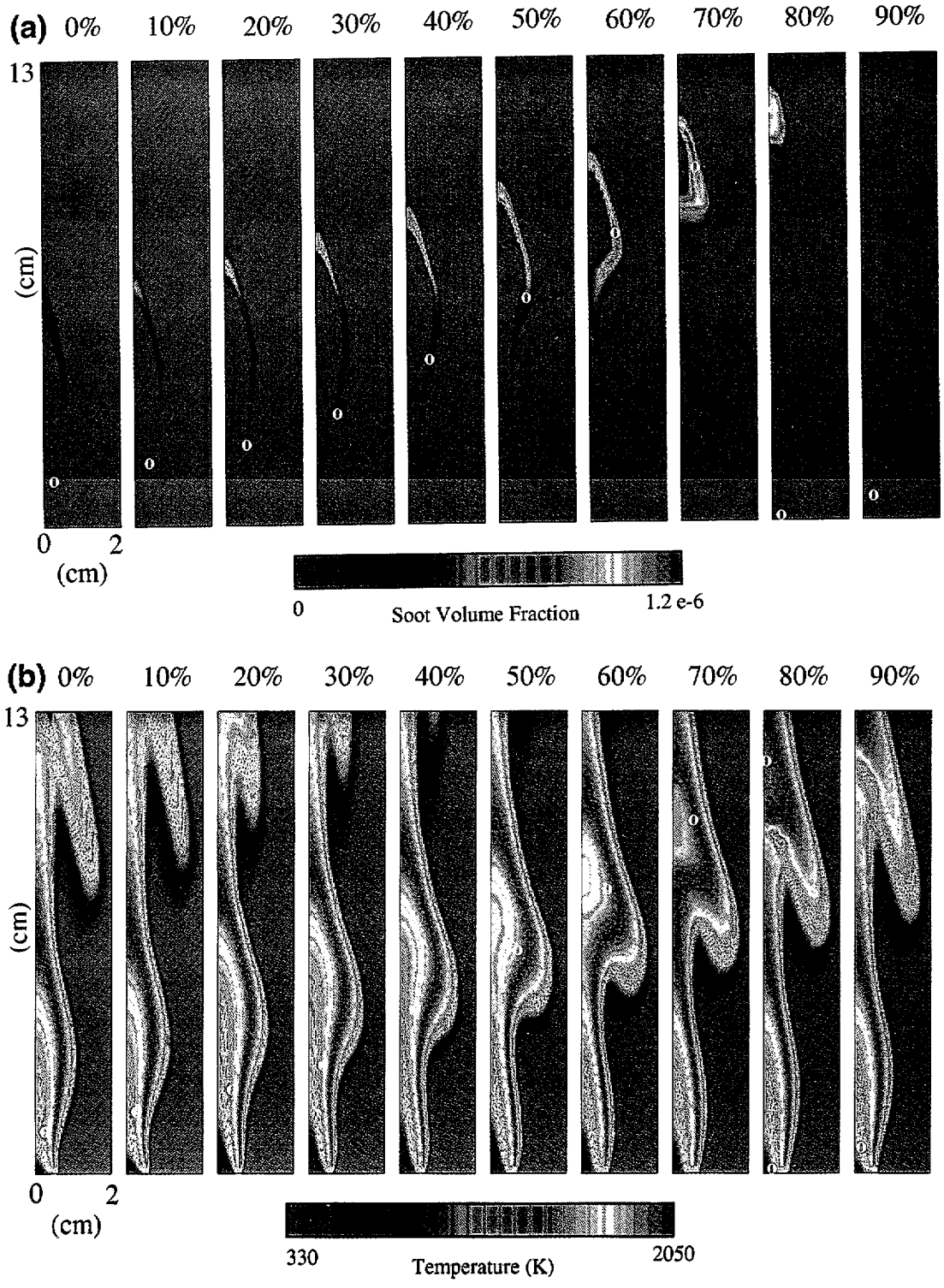

Fig. 6. Images at 10-ms intervals for the computed time-varying CH_4/air diffusion flame in which the fuel inflow was varied with a 10 Hz sine wave with a 75% amplitude. Series (a) corresponds to images of the computed soot volume fraction and (b) corresponds to images of the computed temperature. The white "o" marker in each frame corresponds to the location of the fluid parcel which passes through the region of peak soot volume fraction in the flame.

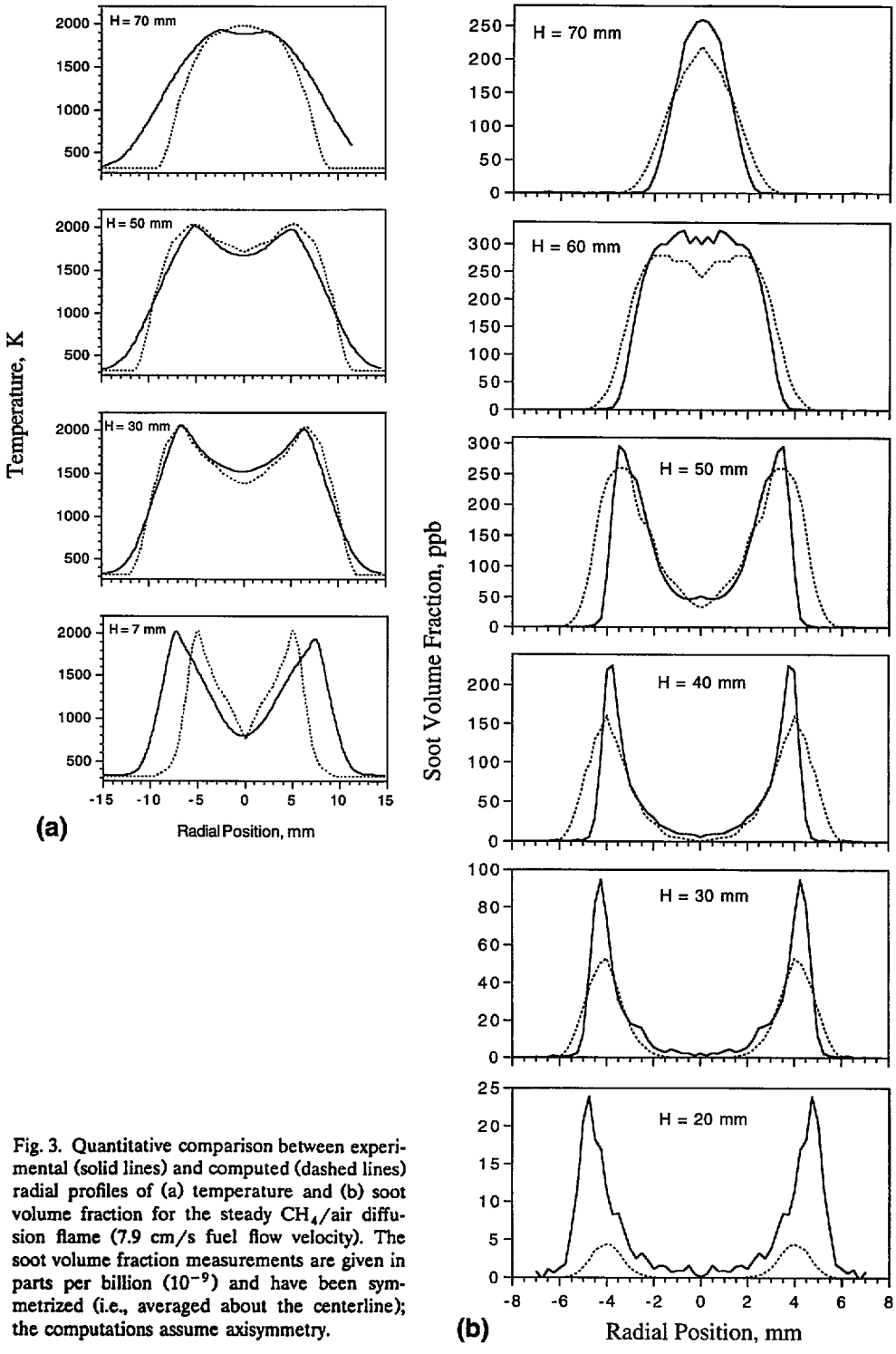

Fig. 3. Quantitative comparison between experimental (solid lines) and computed (dashed lines) radial profiles of (a) temperature and (b) soot volume fraction for the steady CH_4/air diffusion flame (7.9 cm/s fuel flow velocity). The soot volume fraction measurements are given in parts per billion (10^{-9}) and have been symmetrized (i.e., averaged about the centerline); the computations assume axisymmetry.

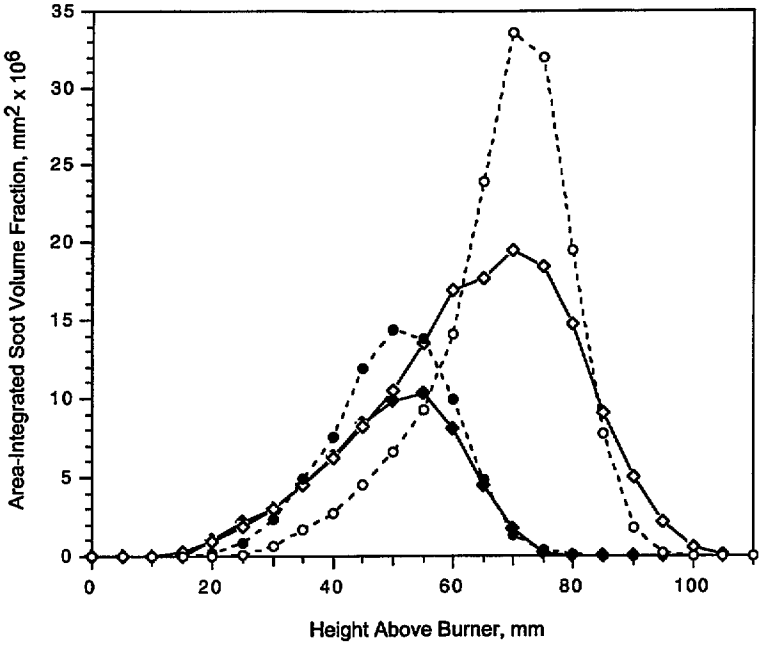

Fig. 4. Area-integrated soot volume fraction as a function of height above the burner for steady CH_4/air flames with fuel flow velocities of 7.9 cm/s (filled symbols) and 10.1 cm/s (open symbols). Diamonds denote experimental results, and circles indicate the computational predictions.

in this flame. At the higher inflow velocities the time-dependent computation predicts a pseudo-steady flowfield; the flame height remains approximately constant with time, but oscillations appear in the flame diameter. Similar trends are evident in comparing the temperature and soot volume fraction profiles as for the 7.9 cm/s flame, except that the computed soot volume fraction develops more slowly at early times and reaches larger values than experimentally measured at higher axial locations. The measured peak soot volume fraction is 5.6×10^{-7} compared with the calculated maximum of 6.8×10^{-7}. As shown in Fig. 4, wider computed soot profiles again result in overestimation of the area-integrated soot volume fraction, but the soot burnout height is well predicted.

Flickering Methane / Air Flame

To experimentally produce the time-varying flame, the methane velocity was modulated by applying a 10-Hz sine wave to a loudspeaker attached to a fuel plenum, maintaining the same *mean* fuel flow velocity (7.9 cm/s) that was used for the steady flame condition [9, 10]. The air coflow velocity was unchanged. Figure 5 shows a series of experimental images for moderate forcing conditions (the excitation voltage on the loudspeaker was 0.75 V) for 10 phase angles, obtained every 10 ms. The continuous outer envelope arises from OH · laser-induced fluorescence signals and denotes the high temperature reaction zone; peak OH · levels are expected to closely follow the stoichiometric contour [35]. As the flame height increases and the flame tip is pinched off, soot scattering signals appear in the interior, fuel-rich regions and become very large. Quantitative measurements have shown that soot scattering in the time-varying flames is enhanced by up to a factor of 35 (depending upon the laser wavelength and polarization) relative to the steady laminar flame burning at the same mean fuel flow velocity [9, 34].

To simulate the acoustic forcing in the computations, a 10-Hz sinusoidal function of varying amplitude (25%, 50%, and 75%) was applied to the fuel inflow velocity. Preliminary hot-wire measurements indicate that the fuel velocity fluctuation in the flickering flame is at

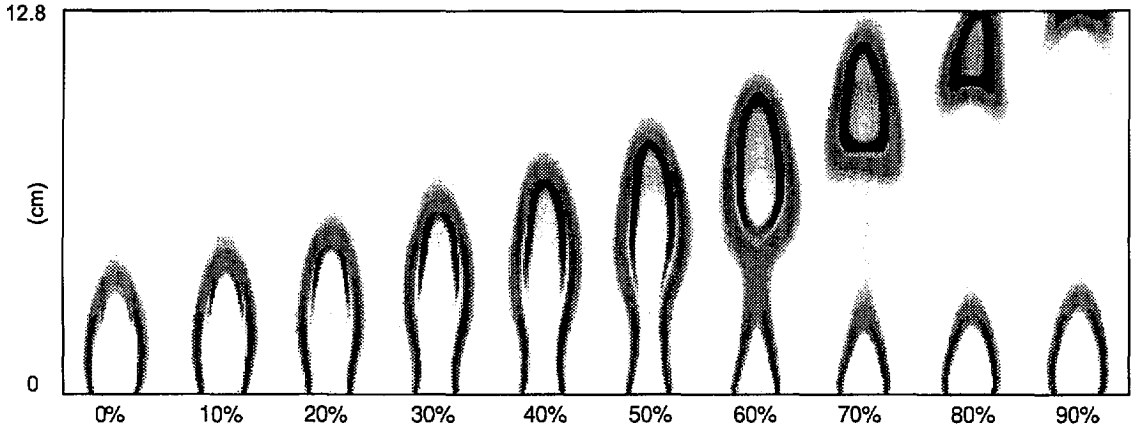

Fig. 5. OH · laser-induced fluorescence and soot scattering images in an acoustically-forced time-varying CH_4/air diffusion flame [9]. Shown are images for moderate forcing conditions (excitation voltage on the loudspeaker is 0.75 V peak-to-peak); the time interval between images is 10 ms.

least 50% for the moderate forcing condition [9]. In addition, predictions from the computations show that the 50% and 75% amplitude conditions give the best qualitative agreement with the experimentally observed flame dynamics. In the discussion to follow the 75% case is emphasized because this computation agrees best with the experimental results in terms of the location of flame clip-off.

Figures 6a and 6b show computed images of the soot volume fraction and the temperature at 10 ms intervals for the 75% amplitude case. The shapes of the simulated and experimental flames are similar, and both exhibit tip clipping. In the clipped portion of the flickering flame, the simulations successfully predict the observed increase in soot volume fraction. The maximum computed soot volume fraction occurs at 70% phase and is approximately four times greater than that measured and calculated for the steady flame with the same mean fuel flow velocity. Some qualitative differences between the computed and experimental flickering flame are apparent. In particular, the computation clips off a smaller portion of unburned fuel at higher heights above the burner. Burnout occurs more rapidly than in the experimental flame.

DISCUSSION

In order to better understand the factors responsible for the enhanced soot production in the flickering flames, fluid parcels were tracked as they followed the convective pathlines in the flame. In particular, the particle which passed through the maximum sooting region was examined, so that the temperature, stoichiometry, and soot volume fraction history could be followed. Figures 7a–7c present these time histories for the computed soot volume fraction, temperature, and stoichiometry, respectively, as a function of the total residence time in the flame beginning at the fuel tube exit.

In Fig. 7a the soot volume fraction is plotted as a function of the residence time for the base case steady flame (7.9 cm/s fuel flow velocity), the taller steady flame (10.1 cm/s fuel flow velocity), and the 25%, 50%, and 75% amplitude flickering flames. Soot inception is defined here to occur at a soot volume fraction of 2×10^{-8}. At this point the particle number density has surpassed $10^9/cm^3$, and the rate of increase of the particle number density has slowed markedly compared to earlier times. The times for soot inception are ~ 42 ms and 43 ms for the 7.9 cm/s and 10.1 cm/s steady flames, and ~ 45, 50, and 53 ms for the 25%, 50%, and 75% amplitude cases, respectively. Temperatures corresponding to these inception times (Fig. 7b) are similar, 1640, 1650, 1730, 1690, and 1700 K, while the equivalence ratios at inception are 7.7, 7.5, 5.8, 5.6, and 4.9, respectively. Hence, these pathlines also suggest that soot inception occurs in flickering flames at slightly higher temperatures and un-

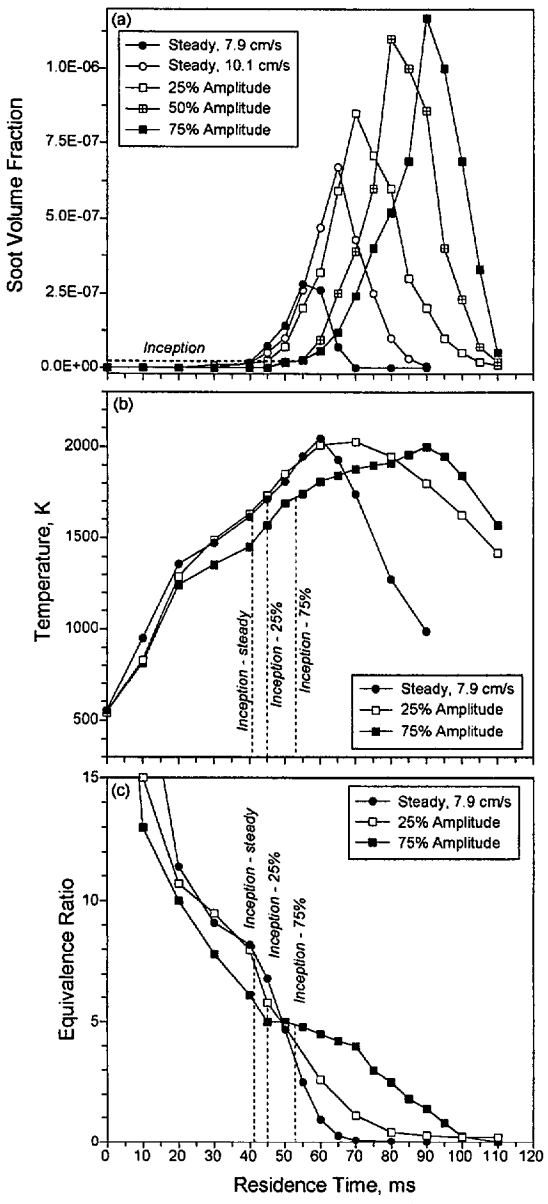

Fig. 7. Computations along pathlines of (a) soot volume fraction, (b) temperature, and (c) equivalence ratio for the steady and flickering flames. At residence times less than 10 ms, near the base of the flame, the equivalence ratio exceeds 40 and has been omitted from Fig. 7c for clarity of presentation.

der somewhat leaner conditions compared to the steady flame. The calculated inception temperatures are consistent with those observed experimentally in axisymmetric methane/air diffusion flames (T = 1740–1760 K at the location of the peak soot volume fraction for early times [33]). In addition, Santoro et al. [36] report T = 1660–1790 K at the location of soot inception in a series of ethylene/air flames.

Since the flickering flames are taller than the steady flames, soot growth occurs over considerably longer times than for steady conditions. The pathlines showing the temperature (Fig. 7b) and equivalence ratio (Fig. 7c) histories reveal that the temperature remains high over an extended time under fuel rich conditions for the flickering flames. Soot production is increased because the temperature and stoichiometries remain favorable for soot growth during this longer residence time. Examination of the corresponding pathline plots for the taller steady flame (10.1 cm/s fuel flow velocity) reveals the same behavior, namely that the residence time for soot growth is significantly longer under temperature-stoichiometry conditions very similar to the base case steady flame (7.9 cm/s fuel flow velocity). Vandsburger et al. [37] have also identified residence time as a key parameter in determining the maximum soot volume fraction in ethylene/air counterflow diffusion flames.

The soot particle number densities calculated along the pathlines of maximum soot concentration are shown for the base case steady flame and the 75% amplitude flickering flame in Fig. 8a. From this information and the corresponding soot volume fractions (Fig. 7a), mean particle diameters can be derived and are presented in Fig. 8b. Since pathline information has not been obtained experimentally, comparisons with measurements can only be made at the temporal and physical location of the maximum soot volume fraction. At this location in the steady flame (55 ms along the pathline), the computed number density is 3.1 $\times$ $10^9/cm^3$ and the mean particle diameter is 56 nm. These values are in excellent agreement with the corresponding quantities derived from a Mie analysis of experimental soot volume fraction and scattering measurements [9, 10]. In the 75% flickering flame the maximum predicted soot concentration occurs at 90 ms along the pathline, where the number density is 8.9 $\times$ $10^9/cm^3$ and the mean particle diameter is 63 nm. These values differ from the Mie analysis results of $\sim 2 \times 10^9/cm^3$ and 105 nm

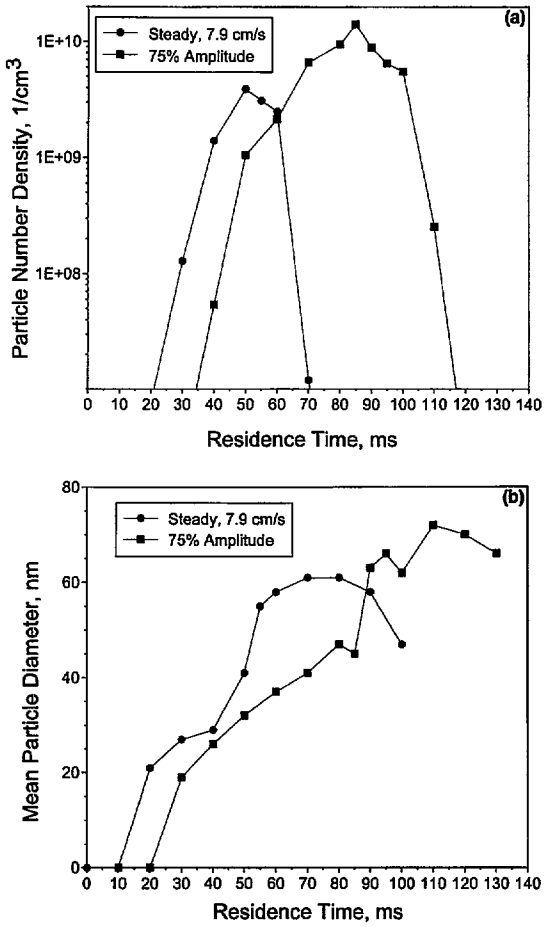

Fig. 8. Calculated soot particle number densities (a) and mean particle diameters (b) along the pathlines of maximum soot concentration for the base case steady flame (7.9 cm/s fuel velocity) and for the 75% amplitude flickering flame.

at the location of maximum soot concentration in the flickering flame. In essence, the numerical simulations with the Syed et al. [12] soot model predict that the enhanced soot concentration in the flickering flame results from the combined effects of soot particle inception and surface growth during the increased residence time in fuel-rich regions. The experimental measurements, in contrast, suggest that soot particle inception diminishes in importance at an earlier time in the flickering flame, such that the enhanced soot concentration relative to the steady flame arises primarily from soot surface growth on the existing particles during the extended residence time.

Based upon the analysis discussed above, the success of the present computation in predicting soot burnout heights in the steady flames is likely due to an unexpectedly large computed rate for soot oxidation by O_2. The Mie analysis of the experimental measurements [9, 10] yields a volume equivalent sphere description of the soot particles, whereas significant agglomeration of small primary particles occurs [30]. As a consequence, one anticipates that the Mie analysis will underestimate the effective surface area for soot oxidation in these methane flames, as has been found for propane and ethylene flames [38, 39]. The computed particle surface area is the same as that given by the Mie analysis for the steady flame and is somewhat larger than the Mie analysis result for the flickering condition, suggesting that the predicted surface area is also underestimated.

The present results represent an important test of the integrated soot model of Syed et al. [12] for combustion conditions more complex than the steady methane/air flame used for establishing the rate coefficients in Eqs. 15 and 16. Syed et al. also utilized a rectilinear Wolfhard-Parker burner geometry in their investigation, compared to the axisymmetric configuration used here. The model's success in predicting the overall enhancement of the soot volume fraction observed experimentally in the flickering flames lends confidence in identifying the extended residence time as the most important parameter affecting increased soot production. To the degree that soot inception and growth in the flickering flame involve new combinations of temperature, stoichiometry, and strain rate, the simplified approach of Syed et al. [12] adequately describes soot production. Because residence time must be accounted for to accurately predict the local soot volume fraction, at least for methane combustion, a description which incorporates only a soot volume fraction/mixture fraction correlation will fail for complex, time-varying conditions.

CONCLUSIONS

Computations of steady and time-varying CH_4/air diffusion flames are used to study the differences in combustion conditions which

lead to the enhanced soot production observed experimentally in flickering flames. Simulations of a steady CH_4/air flame (7.9 cm/s fuel flow velocity) show good qualitative agreement with the experimental results for the soot burnout height and the overall flame shape. Quantitative comparisons between experimental and computed radial profiles of temperature for the steady flame agree at mid-flame heights, but some discrepancies exist near the burner lip and at high axial locations. Comparisons between the experimental and computed soot volume fraction for the steady flame show good agreement for the radial location of the peak soot concentration at all heights and excellent quantitative agreement for the maximum soot concentration. Computation of a taller steady flame (10.1 cm/s fuel flow velocity) predicts a substantial increase in the peak soot volume fraction relative to the shorter flame, in agreement with experimental measurements.

To simulate the acoustic forcing applied to the fuel plenum to produce the experimental flickering flame, a 10-Hz sine wave of varying amplitude (25%, 50%, and 75% amplitude) was applied to the fuel inflow velocity in the computations. The time-varying simulations successfully predict that the maximum soot concentration increases by over four times compared to a steady flame with the same mean fuel and air velocities. Pathlines which trace the history of a fluid parcel as it follows the convective flow through the maximum sooting region show that increased residence time is the most important factor which leads to the enhanced soot production. Mie analysis of the experimental measurements yields particle diameters and number densities in excellent agreement with the calculations for the steady flame, but significantly different for flickering conditions. Nevertheless, the computations demonstrate that the integrated soot model developed from a steady CH_4/air flame by Syed et al. [12] can reasonably predict peak soot levels in time-varying CH_4/air flames which exhibit tip clipping.

The computational work was supported by the Office of Naval Research and the Naval Research Laboratory (NRL), and in part by a grant of High Performance Computing (HPC) time from the DoD HPC Shared Resource Center, CEWES Cray-C90. The NIST effort was supported by the Smoke Dynamics Research Group, Fire Science Division.

REFERENCES

1. Ellzey, J. L. Laskey, K. J., and Oran, E. S., *Combust. Flame* 84:249–264 (1991).
2. Ellzey, J. L., and Oran, E. S., *Twenty-Third Symposium (International) on Combustion*, The Combustion Institute, Pittsburgh, 1990, pp. 1635–1640.
3. Chen, L.-D., Seaba, J. P., Roquemore, W. M., and Goss, L. P., *Twenty-Second Symposium (International) on Combustion*, The Combustion Institute, Pittsburgh, 1988, pp. 677–684.
4. Davis, R. W., Moore, E. F., Roquemore, W. M., Chen, L.-D., Vilimpoc, V., and Goss, L. P., *Combust. Flame* 83:263–270 (1991).
5. Katta, V. R., Goss, L. P., and Roquemore, W. M., *Combust. Flame* 96:60–74 (1994).
6. Takahashi, F., and Katta, V. R., AIAA Paper 93-0456, American Institute of Aeronautics and Astronautics, Washington, D.C., 1993.
7. Kaplan, C. R., Baek, S. W., Oran, E. S., and Ellzey, J. L., *Combust. Flame* 96:1–21 (1994).
8. Kaplan, C. R., Oran, E. S., and Baek, S. W., *Twenty-Fifth Symposium (International) on Combustion*, The Combustion Institute, Pittsburgh, 1994, pp. 1183–1189.
9. Shaddix, C. R., Harrington, J. E., and Smyth, K. C., *Combust. Flame* 99:723–732 (1994) and 100:518 (1995).
10. Shaddix, C. R., and Smyth, K. C., *Combust. Flame*, in press.
11. Moss, J. B., Stewart, C. D., and Syed, K. J, *Twenty-Second Symposium (International) on Combustion*, The Combustion Institute, Pittsburgh, 1988, pp. 413–423.
12. Syed, K. J., Stewart, C. D., and Moss, J. B., *Twenty-Third Symposium (International) on Combustion*, The Combustion Institute, Pittsburgh, 1990, pp. 1533–1541.
13. Stewart, C. D., Syed, K. J., and Moss, J. B., *Combust. Sci. Technol.* 75:211–226 (1991).
14. Kennedy, I. M., Kollmann, W., and Chen, J.-Y., *Combust. Flame* 81:73–85 (1990).
15. Kennedy, I. M., Kollmann, W., and Chen, J.-Y., *AIAA J.* 29:1452–1457 (1991).
16. Villasenor, R., and Kennedy, I. M., *Twenty-Fourth Symposium (International) on Combustion*, The Combustion Institute, Pittsburgh, 1992, pp. 1023–1030.
17. Leung, K. M., Lindstedt, R. P., and Jones, W. P., *Combust. Flame* 87:289–305 (1991).
18. Lindstedt, R. P., *Soot Formation in Combustion: Mechanisms and Models*, Springer Series in Chemical Physics 59, edited by H. Bockhorn, Springer-Verlag, Berlin, chapter 27, pp. 417–441 (1994).
19. Honnery, D. R., Tappe, M., and Kent, J. H., *Combust. Sci. Technol.* 83:305–321 (1992).

20. Kent, J. H., and Honnery, D. R., *Soot Formation in Combustion: Mechanisms and Models*, Springer Series in Chemical Physics 59, edited by H. Bockhorn, Springer-Verlag, Berlin, chapter 12, pp. 199–220 (1994).
21. Honnery, D. R., and Kent, J. H., *Twenty-Fourth Symposium (International) on Combustion*, The Combustion Institute, Pittsburgh, 1992, pp. 1041–1047.
22. Oran, E. S., and Boris, J. P., *Numerical Simulation of Reactive Flow*, Elsevier, New York, 1987, pp. 279–285, 325–327.
23. Patnaik, G., Guirguis, R. H., Boris, J. P., and Oran, E. S., *J. Comp. Phys.* 71:1–20 (1987).
24. Kee, R. J., Warnatz, J., and Miller, J. A., Sandia Report SAND83-8209, Sandia National Laboratories, March 1983.
25. Bilger, R. W., *Combust. Sci. Technol.* 13:155–170 (1976).
26. Bilger, R. W., *Combust. Flame* 30:277–284 (1977).
27. Bilger, R. W., *Twenty-Second Symposium (International) on Combustion*, The Combustion Institute, Pittsburgh, 1988, pp. 475–488.
28. Pivovarov, M. A., Marro, M. A. T., Miller, J. H., and Smooke, M. D., Eastern States Section Meeting of the Combustion Institute (Clearwater, FL), pp. 94–97 (1994).
29. Nagle, J., and Strickland-Constable, R. F., *Proc. Fifth Carbon Conf.* 1:154–164 (1962).
30. Puri, R., Santoro, R. J., and Smyth, K. C., *Combust. Flame* 97:125–144 (1994) and Erratum: *Combust. Flame* 102:226–228 (1995).
31. Kent, J. H., and Honnery, D. R., *Combust. Flame* 79:287–298 (1990).
32. Magnussen, B. F., and Hjertager, B. H., *Sixteenth Symposium (International) on Combustion*, The Combustion Institute, Pittsburgh, 1977, pp. 719–729.
33. Richardson, T. F., and Santoro, R. J., private communication, 1993.
34. Smyth, K. C., Harrington, J. E., Johnsson, E. L., and Pitts, W. M., *Combust. Flame* 94:229–239 (1993).
35. Norton, T. S., Smyth, K. C., Miller, J. H., and Smooke, M. D., *Combust. Sci. Technol.* 90:1–34 (1993).
36. Santoro, R. J., Yeh, T. T., Horvath, J. J., and Semerjian, H. G., *Combust. Sci. Technol.* 53:89–115 (1987).
37. Vandsburger, U., Kennedy, I. M., and Glassman, I., *Twentieth Symposium (International) on Combustion*, The Combustion Institute, Pittsburgh, 1984, pp. 1105–1112.
38. Charalampopoulos, T. T., and Chang, H., *Combust. Flame* 87:89–99 (1991).
39. Puri, R., Richardson, T. F., Santoro, R. J., and Dobbins, R. A., *Combust. Flame* 92:320–333 (1993).

Received 13 June 1995; revised 9 November 1995